Crystallization Mechanisms in New Bismuth Borotellurite Glass-Ceramics

Marine Cholin, Cécile Genevois, Pierre Carles, Mathieu Allix, Julie Cornette, Maggy Colas, Franck Fayon, Vincent Sarou-Kanian, Gaëlle Delaizir, Philippe Thomas, et al.

Crystallization mechanisms

in new bismuth borotellurite glass-ceramics

Marine Cholin[1,2], Cécile Genevois[3], Pierre Carles[1], Mathieu Allix[3], Julie Cornette[1], Maggy Colas[1], Franck Fayon[3], Vincent Sarou-Kanian[3], Gaëlle Delaizir[1], Philippe Thomas[1], Sébastien Chenu[1,4], Vincent Couderc[2], Jean-René Duclère[1,]*

[1] Institut de Recherche sur les Céramiques, UMR 7315 CNRS, Université de Limoges, Centre Européen de la Céramique, Limoges, France

[2] Institut XLIM, UMR 7252 CNRS, Université de Limoges, France

[3] Conditions Extrêmes et Matériaux : Haute Température et Irradiation, UPR 3079 CNRS, Université d'Orléans, F-45071 Orléans, France

[4] Institut des Sciences Chimiques de Rennes, UMR CNRS 6226 - Université de Rennes, 35042 Rennes, France

KEYWORDS: borotellurites, glass-ceramics, chemical demixtion, phase separation

ABSTRACT

The molar composition $30TeO_2$-$40B_2O_3$-$30Bi_2O_3$, doped with $0.5Er_2O_3$, is explored. Starting from a homogeneous glass, new borotellurite glass-ceramics were elaborated after a two-step heat treatment, composed of both nucleation and growth processes. The crucial parameters, determined by Differential Scanning Calorimetry, were the nucleation optimal temperature and duration. The structural modifications occurring while heating, and the related microstructure evolution, were followed by ex situ X-Ray Diffraction and Scanning Electron Microscopy. Mechanisms of the partial crystallization were investigated through Transmission Electron Microscopy observations and local chemical analyses (Energy Dispersive Spectroscopy,

Electron Energy Loss Spectroscopy). Thus, the employed heat treatments formed glass-ceramics composed of boron-free $Bi_2Te_2O_7$ polycrystalline entities dispersed in the boron oxide enriched glassy matrix. The partial crystallization happens therefore concomitantly with the observed chemical demixtion, where boron oxide phase-separates from the bismuth tellurite phase. Besides, Raman spectroscopy and Nuclear Magnetic Resonance data reveal that the overall BO_4/BO_3 ratio of the glass network does not show significant evolution during the partial crystallization. Optical transmission and photoluminescence properties were also measured. For glass-ceramics, the optical transmission strongly drops. Both emission and excitation spectra of Er^{3+} ions, as well as lifetime measurements, highlight the modified environment around the rare-earth ions occurring with the partial crystallization.

INTRODUCTION

Among oxide materials, TeO_2-based glasses (*i.e.* tellurites) are fascinating for a diversity of reasons, such as their low melting point, their excellent third-order nonlinear optical properties [1], as well as their optical transparency up to the mid-infrared range (5-6 µm), therefore covering the important 3-5 µm atmospheric window, where many molecular absorption bands exist [2]. Optical applications of such materials thus include chemical sensors in the medical and environmental domains, fibers, lenses, *etc*…, as regrouped in the following book [3].

Besides, boron oxide is a well-known glass oxide former. Its combination with tellurite glasses leads to the borotellurite family of glasses, which appear to be rather attractive for instance for their radiation shielding properties against ionizing radiations (γ-rays, X-rays, neutrons), as reviewed by Patra and Annapurna in [4]. However, our principal interest lies in another particularity of borotellurites. Indeed, depending on the chemical composition, within the binary TeO_2-B_2O_3 phase diagram, the existence of an immiscibility dome (or gap) was reported in several works, conducted mainly by two research teams [5-8]. Thus, within the appropriate

range of temperature, under such immiscibility dome, the TeO_2-B_2O_3 system will normally undergo some liquid-liquid phase separation that will lead, after quenching, to final chemically demixed glasses (with some regions richer in TeO_2 and others richer in B_2O_3). Consequently, one of our inspiration is that such type of phase-separated glass micro/nanostructures could potentially be further used for elaborating glass-ceramics, as it was for instance accomplished by Bhattacharyya *et al*. for aluminosilicates [9] or by Chenu *et al*. for gallogermanates [10].

Borotellurite ternary systems were then further investigated, and firstly, we are specifically interested in reviewing the contributions dealing with glasses issued from the TeO_2-B_2O_3-Bi_2O_3 system. Kaschieva *et al*. did some pioneer work on TeO_2-B_2O_3-M_2O_3 systems (where M_2O_3 = Al_2O_3, Ga_2O_3, Sc_2O_3, La_2O_3, Bi_2O_3) [11]. In particular, they conducted Transmission Electron Microscopy (TEM) observations of the microstructure of the elaborated glasses. Their approach allowed to separate regions of the diagram where the elaborated glasses were homogeneous (labelled as the one-phase glass region) from regions where the glasses were phase separated (labelled as the two-phase glass region). Amazingly, for the $70TeO_2$-$20B_2O_3$-$10Bi_2O_3$ (%mol) composition, which stands within the one-phase glass region of the ternary diagram, their TEM data clearly revealed the occurrence of some phase separation, characterized by the formation of micro-aggregates or immiscibility droplets dispersed in a one-phase glass matrix, thus in disagreement with the "one-phase" classification employed. Such "ambiguity" constituted another reason which motivated us to carefully reinvestigate this TeO_2-B_2O_3-Bi_2O_3 system. In the work conducted by Hasegawa within the TeO_2–B_2O_3-Bi_2O_3 ternary system [12], in terms of glass forming domain, he retrieved similar results than Kaschieva *et al*. [11]. He investigated mainly the linear and nonlinear optical properties of the fabricated glasses. Zhao *et al*. established the glass forming domain in the TeO_2-B_2O_3-Bi_2O_3 ternary system, for boron oxide concentrations lower than 40 mol.% [13]. They focused on optical properties and thermal stability of the glasses, and studied the influence of the Bi_2O_3 content on the structure.

Kaur *et al.* investigated, by ^{11}B MAS-NMR, Fourier-Transform InfraRed (FTIR) and Raman spectroscopies, the structure of bismuth tellurite and bismuth borotellurite melt-quenched glasses (xBi_2O_3-yB_2O_3-$(100-x-y)TeO_2$ (where x = 20 mol.% and $20 \leq y \leq 40$ mol.%) [14]. In particular, they reported some study on the incorporation of B_2O_3 into the bismuth tellurite system, which enhances significantly the glass forming ability and allows the fabrication of transparent bulk bismuth borotellurite glass samples at common quenching rates. By doing so, the authors avoided the formation of the $Bi_2Te_4O_{11}$ crystalline phase. Saddeek *et al*. looked into the elastic and structural properties, as well as the thermal characteristics of five glasses in the TeO_2–B_2O_3–Bi_2O_3 system [15]. The authors reported mainly on the Bi_2O_3 glass former role, based on their FTIR analysis. Sm^{3+}-doped bismuth borotellurite glasses were also synthesized by Lakshmi *et al*., and the corresponding photoluminescence properties were measured [16]. Finally, Amat *et al*. published on $[(TeO_2)_{70}(B_2O_3)_{30}]_{100-x}(Bi_2O_3)_x$ glasses, and examined the influence of the bismuth oxide content on the structural/optical properties [17]. With the Bi_2O_3 concentration increase, the authors have shown that the average boron-boron distance decreases. Secondly, we wish to concentrate on the literature treating the formation of glass-ceramics within such TeO_2-B_2O_3-Bi_2O_3 ternary system and also within TeO_2-B_2O_3-Bi_2O_3-based systems. Elkhoshkhany *et al*. investigated the crystallization of bismuth borotellurite glasses [18]. In particular, the authors synthesized new glass-ceramics containing the $BiTe_3O_{7.5}$ cubic crystalline phase. To further incorporate TiO_2 (the latter acting as a nucleating agent which favours the precipitation of micro crystals) induces the formation of orthorhombic $Bi_4Ti_3O_{12}$.$4TeO_2$ along with tetragonal Bi_2O_3 phases. Both Scanning Electronic Microscopy (SEM) and TEM observations of the resulting microstructures were also provided in this article. Shaaban *et al*. elaborated by melt-quenching some glass samples of the following compositions ($(90-x)TeO_2 – 10B_2O_3 – xBi_2O_3$, and where $40 \leq x \leq 80$ mol. %) [19]. Through a controlled heat treatment, they prepared some glass-ceramics with the nano-size cubic $BiTe_3O_{7.5}$ as the

main crystalline phase, which was found to coexist with both Bi_2O_3 and TeO_2 crystalline phases. Based on the TEM images of the final microstructures of the glass-ceramics, the authors showed that, depending on the composition, the size of crystals varied from ~ 65 nm up to ~ 350 nm. Very recently, Mhareb *et al.* studied the effect of gamma rays on the structural and optical properties, as well as on the durability of new glass and glass–ceramic of the following composition: $10ZnO–34.5B_2O_3–34.5TeO_2–20Bi_2O_3–1Nd_2O_3$ [20]. For their glass-ceramic sample irradiated at different doses, it is worth mentioning that the authors evidenced only the presence of the unique orthorhombic $Bi_2Te_2O_7$ crystalline phase. Finally, for the $60TeO_2$-$20B_2O_3$-$20Bi_2O_3$ composition, via an adapted single step heat treatment, we recently succeeded to elaborate highly transparent glass-ceramics thanks to the partial and controlled crystallization of the anti-glass $Bi_2Te_4O_{11}$ phase [21]. With longer heat treatments, TEM observations clearly revealed the existence of isolated polycrystalline $Bi_2Te_4O_{11}$ entities dispersed in a heterogeneous residual glassy matrix, where two separate amorphous regions of a different composition coexist, therefore strongly suggesting the occurrence of a chemical demixtion process. However, due to the instability of the samples under the electron beam, it was unfortunately impossible to go further and be more specific about the spatial repartition of the chemical elements, especially boron.

Therefore, in comparison with our former contribution on borotellurites [21], this paper focuses on the specific $30TeO_2$-$40B_2O_3$-$30Bi_2O_3$ composition, which is poorer in TeO_2, richer in both B_2O_3 and Bi_2O_3, and from which it is expected to obtain a one-phase glass based on [11]. By using an adapted two-step (nucleation / growth) heat treatment, starting from the parent glass, we demonstrate the possibility to elaborate new glass-ceramics. Based on TEM investigations (nanoscale observations, local chemical analysis conducted in Scanning-TEM mode and using Electron Energy Loss Spectroscopy (EELS), we bring some insights about the crystallization mechanisms involved and provide some clear evidence for a chemical demixtion phenomenon.

EXPERIMENTAL SECTION

In this work, glasses with the molar composition $30TeO_2$-$40B_2O_3$-$30Bi_2O_3$ doped with $0.5Er_2O_3$ (labeled TBB-Er in the rest of the paper) were specifically elaborated by using the melt-quenching method. Batches of 3g were prepared from the following initial powders: Bi_2O_3 (Sigma-Aldrich, 99.99%), TeO_2 (Todini, 99.9%), H_3BO_3 (Strem Chemicals, 99.99%) and Er_2O_3 (Sigma-Aldrich, 99.9%). Powders were weighted in stoichiometric proportions, intimately mixed and transferred into platinum crucibles. After that, the mixtures were melted at 850°C during 75 min, homogenized every 15 min, and quenched on a preheated hot plate (320°C) without any casting. The bulk glasses were further demolded from the platinum crucibles at ambient temperature. To relax the mechanical constraints resulting from the quenching process, an annealing treatment was performed at T_g-30°C during 6h and the sample was then slowly cooled down to room temperature. The thermal behavior of the quenched glass was evaluated by Differential Scanning Calorimetry (DSC) under air, by using a TA instrument AQ20 equipment. This analysis was done on about 8-10 mg of material, for both bulk and powder samples. DSC runs were collected from room temperature up to 550°C (or 575°C if necessary), with a heating rate of 10 $K.min^{-1}$ to determine the characteristic temperatures of the elaborated glass. In order to fabricate glass-ceramics, a two-step heat treatment under air was employed to partially crystallize the parent glass:

(i) the nucleation step was conducted at 405°C during 2h,

(ii) the growth step was carried out at 450°C during different durations, up to 2h. Before and after the diverse heat treatments, X-Ray Diffraction (XRD) measurements were performed at room temperature using a D8 Advance Bruker diffractometer equipment, which delivered the CuK_α radiation (λ_{Cu} = 1.5406 Å) at the surface of glass and glass-ceramic bulk polished samples, to either control the amorphous nature or identify the crystalline phases. Rietveld refinements

were conducted using the JANA2020 software [22], on the powder issued from the grinded glass-ceramic sample obtained after 2h of heat-treatment at 450°C.

Employing an InVia Reflex Renishaw Raman spectrophotometer, micro-Raman spectroscopy experiments were performed on powders issued from the undoped quenched and nucleated glasses and from all the undoped glass-ceramic (GC) samples heat-treated from 30 min to 2h. The photoluminescence of Er^{3+} ions indeed hides relevant signals arising from structural modifications, justifying why we had to synthesize the "equivalent" undoped samples. The spectra were collected from ~ 200 to 1850 cm^{-1}, using a x10 objective and a 532 nm excitation wavelength, under a continuous wave laser power of ~ 4 mW at the sample. Each displayed spectrum finally results from the average of four different sets of collected data points.

^{11}B solid-state NMR experiments were conducted on Bruker spectrometers operating at magnetic fields of 20.0 T and 9.4 T (^{11}B Larmor frequency of 272.8 and 128.4 MHz). ^{11}B quantitative MAS spectra were recorded at 20.0 T using boron-free Doty probehead and 4 mm rotors with spinning frequencies from 15 to 17 kHz. A short flip angle ($\pi/14$) and a recycle delay of 3s were used to ensure quantitative conditions. Additional ^{11}B MQMAS spectra were recorded at 9.4 T with a 3.2 mm Bruker probehead using the Z-filter sequence [23]. A radiofrequency field strength of 160 kHz was used for excitation and reconversion of triple-quantum coherences. The spinning rate was set to 20 kHz and the recycle delay to 1s. ^{11}B chemical shifts were referenced relative to $BF_3.Et_2O$ at 0 ppm.

A Quanta 450 FEG Scanning Electron Microscope (SEM) was used to observe the microstructure of the three GC samples, synthesized after 45 min, 1h and 2h of heat-treatment at 450°C. The bulk samples were optically mirror-polished, prior to the observations. The surface crystalline fraction was estimated by image analyses with the ImageJ software [24]. The different steps of the image processing consisted in applying: i) a threshold in grey level, ii) a binarisation step followed by iii) a segmentation to correctly identify the border between the

polycrystalline particles and the residual glassy matrix. Elementary analysis was carried out using an Energy-dispersive X-ray Spectroscopy (EDS) detector mounted onto a SEM JEOL IT 300 LV. The macroscopic Bi/Te ratio was particularly controlled on several nucleated glassy samples: the average collected data served as a reference in order to further "calibrate" the local chemical EDS analysis conducted inside the transmission electron microscope.

The nanostructure of both the nucleated glass and the glass-ceramic samples resulting from the heat treatment during 1h at 450°C was observed by TEM. Selected Area Electron Diffraction (SAED) patterns were recorded for checking crystallinity and accessing some structural information. Moreover, the chemical composition, and in particular the Bi/Te ratio, were obtained by EDS analyses, completed by High Angle Annular Dark Field Scanning Transmission Electron Microscopy (HAADF-STEM) imaging. In addition, the spatial repartition of Boron within the GC sample was probed by EELS analyses. For all these TEM characterizations, ultra-thin lamellae (thickness below 100 nm) were prepared by Focused Ion Beam (FIB, ZEISS Crossbeam 550). Due to the difficulty to observe these sensitive samples under the electron beam, two different microscopes were used for the TEM characterizations:

(1) a JEOL 2100F microscope operated at 200kV, with a double tilt liquid nitrogen cooling holder,

(2) a JEOL ARM200F cold FEG microscope operated at 80kV, equipped with a double spherical aberration corrector and fitted with a JEOL SDD CENTURIO EDS system and a Gatan Imaging Filter (GIF) Quantum for the chemical analyses.

Optical properties were as well evaluated. UV-visible-Near InfraRed (NIR) and FTIR spectrometers were employed for the optical transmission measurements of polished (thickness = 0.70 ± 0.05 mm) samples (nucleated glass, and glass-ceramics). The experiments were executed respectively in the 200-3300 nm range under normal incidence, using a Cary 5000

spectrophotometer from Varian company (dual beam configuration) and in the 1500 – 6000 nm range using a Nicolet Is10 FTIR spectrometer. Only the 200-6000 nm range is displayed.

Room temperature visible photoluminescence (PL) properties were measured on polished bulk glasses and glass-ceramics, using a Horiba-Jobin-Yvon Fluorolog 3 spectrofluorimeter, operated in reflective geometry. The fluorescence emission spectra were collected in the 1400-1650 nm range, which comprises the $^4I_{13/2}$-$^4I_{15/2}$ electronic transition of Er^{3+} ions. The data step was set to 0.5 nm, with an emission slit size of 1.5 nm, using an excitation wavelength fixed at 978.5 nm. Photoluminescence decay curves were also recorded, by fixing an initial delay of 50 µs in order to completely get rid of any residual stray light coming from the excitation pulse. Some values were fixed: 15 ms for the maximum delay time, 50 µs as the time interval step, and a sample window equal to 2 ms.

RESULTS AND DISCUSSION

Thermal characteristics of the quenched and nucleated glasses

The specific TBB-Er ($30TeO_2$-$40B_2O_3$-$30Bi_2O_3$ doped with $0.5Er_2O_3$) glass molar composition was investigated. After synthesis, DSC thermograms were collected for bulk and powdered samples. The corresponding data, presented in **Figure 1**, are different and indicate preferential surface crystallization, as the latter occurs at a lower temperature than volume crystallization.

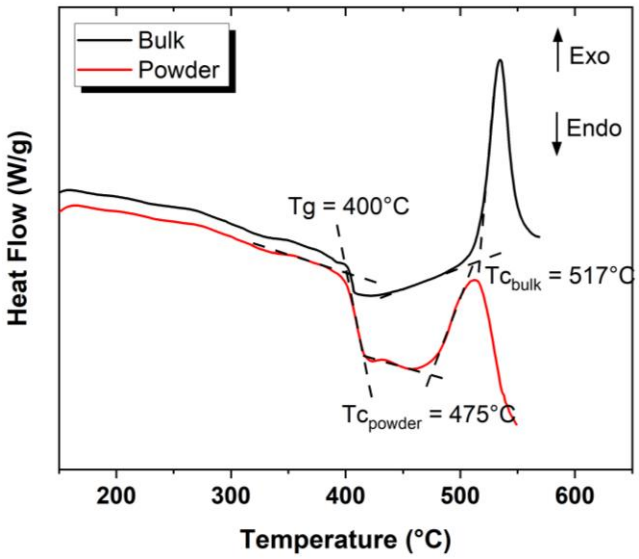

Figure 1: DSC thermograms (bulk and powder) from the initial glass of the TBB-Er composition (heating rate of 10 $K.min^{-1}$). The T_g and onset T_c temperatures are indicated.

Hence, the simple use of a single heat-treatment (which would combine both nucleation and growth steps) will not provoke here any volume crystallization, as opposed to our previous work conducted on the $60TeO_2$-$20B_2O_3$-$20Bi_2O_3$ composition [21]. Thus, to generate volume crystallization, a different approach is needed. The two-step glass crystallization is a powerful method to design transparent glass-ceramics [25]. It involves firstly a nucleation step (conducted at lower temperature) to create small nuclei disseminated within the whole volume of the sample, followed secondly by a growth step (conducted at higher temperature) to control the crystal size. This requires preliminary differential thermal analyses in order to determine the optimal nucleated temperature and time [26-29], and such approach is frequently qualified as the Kissinger method [26]. For tellurite materials, several studies have shown that applying such a two-step heat treatment allowed maintaining a good optical transparency [30-31].

Therefore, for our current borotellurite samples, such Kissinger method was applied, and a nucleation study was undertaken. Firstly, a series of bulks with similar masses (8.3 ± 0.5 mg) were subject to various DSC runs, starting from ambient temperature up to 550°C (heating ramp

of 10°C/min), with for each run a 30 min isotherm set at a different temperature varying from 390°C (10°C before T_g) up to 450°C, by increments of 5°C. If the formation of nuclei is successful, the further crystallization process will be facilitated, then inducing a shift of Tp (Tp being the temperature where the amplitude of the crystallization peak is maximum) towards lower temperature. The optimal nucleation temperature (T_{opt}) was finally established at the maximum of the curve 1/Tp displayed as a function of the isotherm temperature (**Figure 2-a**). Secondly, bulks from the same sample were subject to another series of isothermal DSC analysis, where the isotherm temperature was set this time at T_{opt}, for a duration varying from 15 min up to 120 min. The optimal nucleated time (t_{opt}) is then obtained when the 1/Tp curve reaches a rather stable value (**Figure 2-b**). To summarize, optimal nucleation parameters correspond to a dwelling time of 2h at a temperature of 405°C.

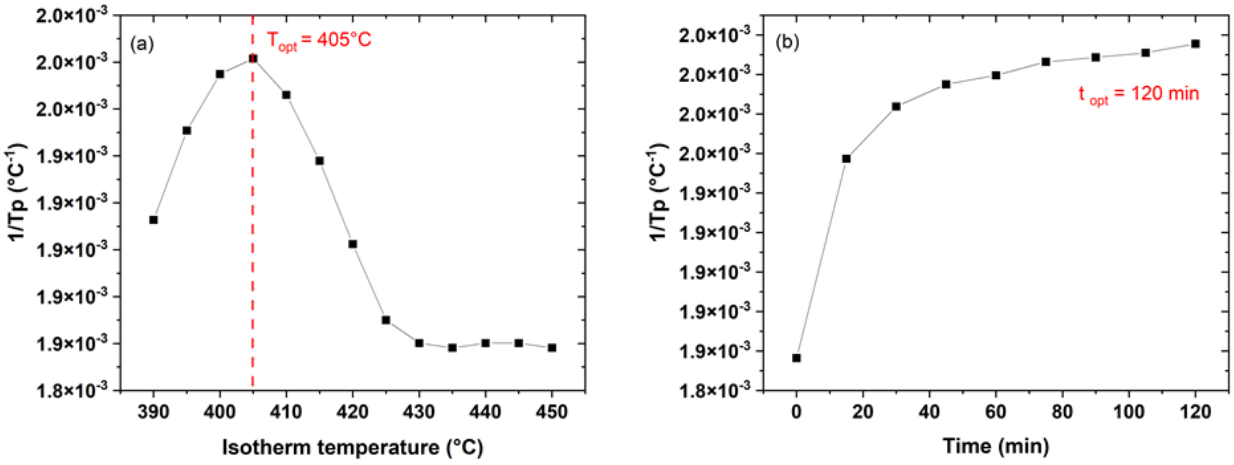

Figure 2: 1/Tp nucleation curves as a function of the isotherm temperature, for an isothermal time of 30 min (a) and as a function of time for T = T_{opt} = 405°C (b), for the TBB-Er glass.

Finally, the nucleated glass was thermally characterized. Bulk and powder DSC signals are this time almost similar, suggesting that volume crystallization is now competing with surface crystallization (**Figure 3**). One can access the glass transition temperature, T_g = 400°C, as well as the first crystallization temperature, T_c = 481°C (onset value). Obviously, this value of T_g is

comparable to values measured for various glass compositions fabricated within the TBB ternary diagram [14], [21]. Moreover, the glass stability is evaluated through the Dietzel criterion, where $\Delta T = T_c - T_g = 81°C$. Thereby, the growth temperature, which corresponds to the second heat treatment to be defined, should stand between the nucleation temperature and the onset crystallization temperature. Thus, different glass-ceramics were produced, starting each time from a nucleated glass which was further brought at the growth temperature of 450°C (*i.e.* T_c - 31°C), during times ranging from 30 min up to 2h. After polishing down to a thickness of 0.70 ± 0.05 mm, samples were characterized.

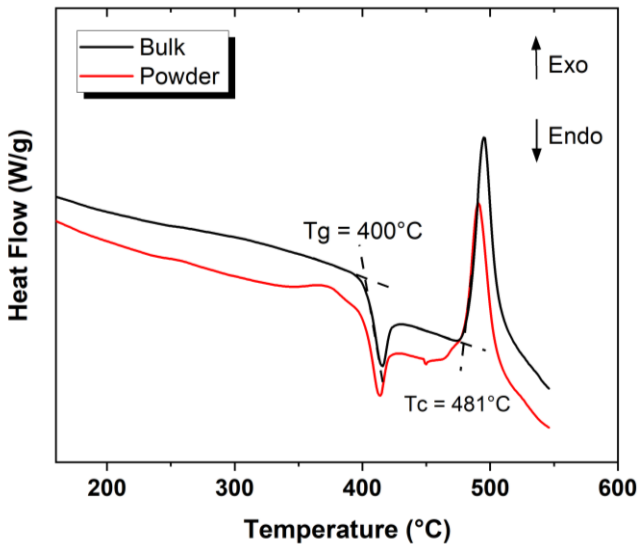

Figure 3: DSC thermograms (bulk and powder forms)

recorded for the nucleated (2h at 405°C) TBB-Er glass (heating rate of 10 $K.min^{-1}$).

Structural characterizations of borotellurite glass-ceramics

First, the amorphous nature of the nucleated glass was controlled by XRD measurements, as shown in **Figure 4-a**. Heat-treatments performed at 450°C, under atmospheric conditions, successfully lead to the fabrication of glass-ceramics (**Figure 4-a**), with the crystallization of the unique $Bi_2Te_2O_7$ crystalline phase [32]. A zoom in **Figure 4-a** (see **Figure S1**) in the 15-40° 2θ range reveals that the first signs of the crystallization occur after at least 45 min at 450°C,

with the appearance of the first Bragg peak at 2θ ~ 27.76° in the corresponding XRD pattern (the main Bragg reflection of the $Bi_2Te_2O_7$ phase – JCPDS file 04-011-4809). With increasing the heat treatment time at 450°C, the crystalline phase will further develop. Amazingly, it is noteworthy that the $Bi_2Te_2O_7$ crystal phase corresponds to a Bi/Te ratio equal to 1, whereas the initial glass composition corresponds to a quantity of bismuth which is twice that of tellurium. This point will be discussed later in this paper, in light of the TEM investigations.

In parallel, a heat treatment at 450°C during 1h was performed on the quenched glass without any nucleation step, and no crystallization at all was detected by XRD. This highlights the importance and necessity of such nucleation step to promote crystallization.

Powder XRD data of the glass-ceramic sample obtained after the nucleation step (2h at 405°C) and the heat treatment during 2h at 450°C can be well indexed with the orthorhombic $Bi_2Te_2O_7$ phase [32], where the known lattice constants are: a = 22.794 Å; b = 5.526 Å; c = 22.065 Å, with the Pbcn(60) space group (JCPDS file 04-011-4809). From these initial reference parameters and using 4 different positions for Bi and Te atoms, as well as 14 positions for O atoms [32], a Rietveld refinement was performed. Only cell parameters, powder profile function parameters and cationic positions were refined. The experimental data (red dots), the calculated data (black curve) and the difference between the model and the experimental data (blue curve) are shown in **Figure 4-b**. The refined data are as follows: (i) lattice constants: a = 22.800 Å, b = 5.535 Å, c = 22.017 Å; (ii) cell angles: $\alpha = \beta = \gamma = 90°$; (iii) cell volume: 2778.6 $Å^3$

Thus, the refined parameters are close to the reference values (maximum deviation of - 0.22% for the c lattice constant). The moderate observed differences suggest therefore only some very small cell distortion, which could be for instance related to a small variation in the tellurium and/or bismuth site occupancy. The actual experimental composition could then slightly differ from the ideal stoichiometric $Bi_2Te_2O_7$ phase. This point will be further discussed in connection with the TEM data.

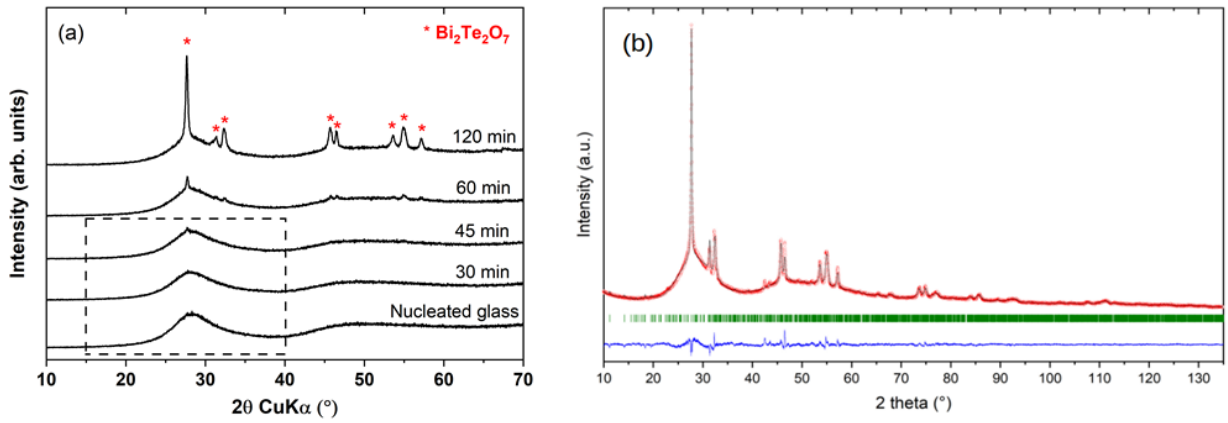

Figure 4: (a) XRD patterns collected for the sample solely nucleated and for the nucleated samples with further growth treatment at 450°C, during different dwelling times: from 30 min up to 2h. The $Bi_2Te_2O_7$ phase (JCPDS file 04-011-4809) is used for indexation (red * labels). The dashed rectangle highlights the angular range displayed in the supplementary Figure S1. (b) XRD Rietveld refinement of the structural parameters conducted on the powder of the glass-ceramic sample elaborated after 2h at 450°C. The goodness of fit (GOF) and the reliability parameters are given here: GOF = 1.86, Rp = 3.16 %, wRp = 4.13 %.

Raman spectroscopy was used to characterize the local structure of these borotellurite samples (glasses and glass-ceramics). As emphasized in the experimental section, due to the photoluminescence of Er^{3+} ions, we had to synthesize the "equivalent" undoped samples, in order to be able to access relevant structural modifications occurring during the nucleation and growth steps. Measurements were thus collected on the undoped quenched and nucleated glasses, as well as on all the undoped samples heat-treated at the growth temperature during the same interval of time (from 30 min up to 2h). As shown in **Figure 5-a**, data were baseline corrected (linear baseline) and normalized to 1 after dividing by the integrated signal on all the wavenumber range. First, it is important to underline that the Raman spectrum of the nucleated glass almost overlaps with that of the initial quenched glass, showing only minute differences simply related to the inherent dispersion of the measurements (each displayed Raman spectrum

results from the average of four sets of collected data points). Then, it should be also noted that Raman spectra of quenched and nucleated glasses are globally rather similar to the Raman spectra obtained by Kaur *et al*. for chemical compositions close to the one under study [14].

Based on previous works (like [21]), all the modes can be identified and attributed to:

- Te-O-Te and Te-O-Bi bridges, as well as isolated TeO_3 pyramidal units ($[TeO_3]^{2-}$ ortho-ions) [33] (large band located between ~ 265 and ~ 550 cm^{-1}, and peaking up around 350-400 cm^{-1})
- stretching vibrations within TeO_4 and TeO_3 units around 660 cm^{-1} and 750 cm^{-1}, respectively
- beyond 800 cm^{-1} and up to 1550 cm^{-1}, despite the exceptionally high Raman intensities observed for glasses composed of heavy metal oxides [34] (in close connection with the existence of an electronic lone pair for both Te and Bi elements), one can still evidence all the vibrations related uniquely to boron oxides BO_n (n = 3 and 4) structural entities [35-36]. The different vibration modes located at ~ 930, ~ 1070-1075, ~ 1220, ~ 1315 and ~ 1415 cm^{-1} can be exhaustively detected.

More precisely, using the following notation employed in [36], where Ø and O^- denote respectively bridging and non-bridging oxygen atoms, the subsequent attribution is possible:

- the modes at ~ 900 and ~ 1070-1075 cm^{-1} might correspond to the stretch vibration of the B–Ø bond in $BØ_4^-$ units,
- the mode at ~ 1220 cm^{-1} could be explained by the stretch vibration of the B–O–B bridge in pyroborate units,
- the mode at ~ 1315 cm^{-1} (main Raman band in this spectral range) probably corresponds to the stretch vibration of the terminal $B–O^-$ bond in pyroborate units,
- the mode at ~ 1415 cm^{-1} is likely due to the stretch vibration of the $B–O^-$ bond in $BØ_2O^-$ units.

Finally, three main observations can be made, based on this set of Raman data:

(i) up to 1h of heat treatment at the growth temperature, almost no modification seems to happen, and beyond that time, a drastic spectral change occurs. Such change is on one hand

characterized by the modification of the large band located between ~ 265 and ~ 550 cm^{-1}, with its sharpening into two modes located at ~ 300 and ~ 350 cm^{-1}, attributed to angular deformation of TeO_3 pyramids [33]. On another hand, the main spectral modification happens with the clear narrowing of the two bands located at ~ 660 and ~ 750 cm^{-1}, respectively related to the stretching vibrations within TeO_4 and TeO_3 units, as mentioned above. Besides, the intensity of each mode is increased, but in particular, the intensity of the mode located at 750 cm^{-1} is strongly reinforced, thus in complete agreement with the crystallization of the $Bi_2Te_2O_7$ structure which is known to be mainly composed of isolated TeO_3 pyramidal units [32].

(ii) for the GC sample elaborated after 2h spent at 450°C, the relative intensity of BO_4 / BO_3 borate structural units (see emphasis in **Figure 5-a**) in respect with that of tellurite TeO_4/TeO_3 units clearly drops. This is another manifestation of the partial crystallization. However, it must be stressed that despite these changes, the borate structural glassy network appears in fact only little affected by the partial crystallization. Indeed, the BO_3/BO_4 ratio of borate structural units does not seem to really evolve, and this fact will be accurately confirmed by ^{11}B NMR data.

(iii) beyond a time of 45 min spent at 450°C, some clear shift of the position of the mode related to the stretching vibrations within TeO_3 units is noticed towards higher wavenumbers. The latter is highlighted in **Figure 5-a** by the red arrow and better displayed in **Figure 5-b**. Indeed, the position of the maximum amplitude of this mode (determined by curve fitting of modes between 540 and 840 cm^{-1}) will first remain constant at ~ 748 cm^{-1} up to 45 min of heat treatment before slightly shifting to 749 cm^{-1} (1h). Beyond that time (2h sample), a strong shift up to 754 cm^{-1} is clearly evidenced. It is noteworthy that such modifications perfectly match temporally with the XRD data and the first appearance of the main Bragg peak of the $Bi_2Te_2O_7$ phase. In addition, the consequent shift (6 cm^{-1}) noticed is by far larger than the resolution of our spectrometer (2.5 cm^{-1}) and thus constitutes another sign of the drastic modification occurring beyond 1h of heat treatment at such growth temperature.

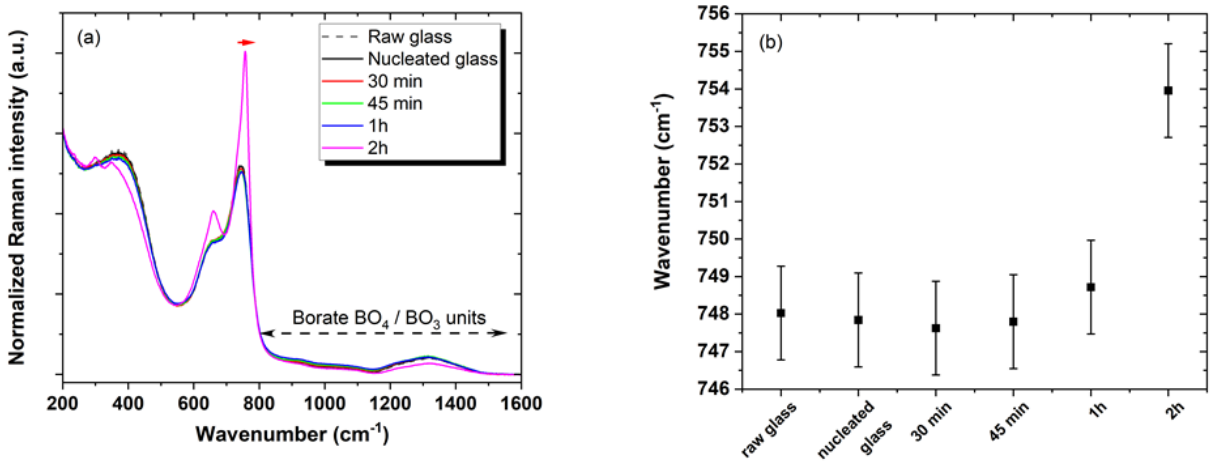

Figure 5: (a) Normalized Raman spectra (after baseline correction) collected for the quenched and nucleated glasses (2h at 405°C), as well as for the samples nucleated and heat-treated from 30 min up to 2h at 450°C. The spectral range of BO_4 / BO_3 units is emphasized and the red arrow highlights the shift of the stretching vibration mode of TeO_3 units. (b) Spectral position for the maximum amplitude of this mode for all the samples. The error bars correspond to a value of ± 1.25 cm^{-1} in concordance with the 2.5 cm^{-1} spectral resolution.

Structural variations in the glass matrix during nucleation and growth processes were also investigated using solid-state ^{11}B NMR. Since the presence of Er^{3+} ions should result in a significant paramagnetic broadening of the ^{11}B NMR signal, experiments were carried out on both Er^{3+}-doped and undoped samples. As shown in **Figure 6**, ^{11}B MAS NMR spectra of undoped samples recorded at 20.0 T clearly reveal the presence of two resonances centered at 16 and 1 ppm, corresponding to BO_3 and BO_4 structural units respectively. No change in line shape is observed during the nucleation and growth steps, indicating that boron atoms remain in the glass matrix and are not involved in the crystalline phase. Furthermore, quantitative analysis of the spectra (including central and satellite ^{11}B transitions) shows no significant variation in the relative BO_3 and BO_4 populations during the different heat treatments. However, the observation of a relatively constant overall BO_3/BO_4 ratio for all samples does

not rule out the presence of structural fluctuations of the glassy matrix in the vicinity of the $Bi_2Te_2O_7$ crystals during the growth process. For Er^{3+}-doped materials, a quantitative analysis accounting for sample weights reveals that up to about 39% of the ^{11}B nuclei suffer from paramagnetic bleaching and are not observed in the ^{11}B MAS spectra. The remaining observed BO_3 and BO_4 resonances are also broadened by paramagnetic interactions with Er^{3+}. Taking this effect into account, the BO_3/BO_4 ratio obtained from spectrum simulations is found to remain nearly constant during the nucleation and growth stages, as observed in the case of undoped materials.

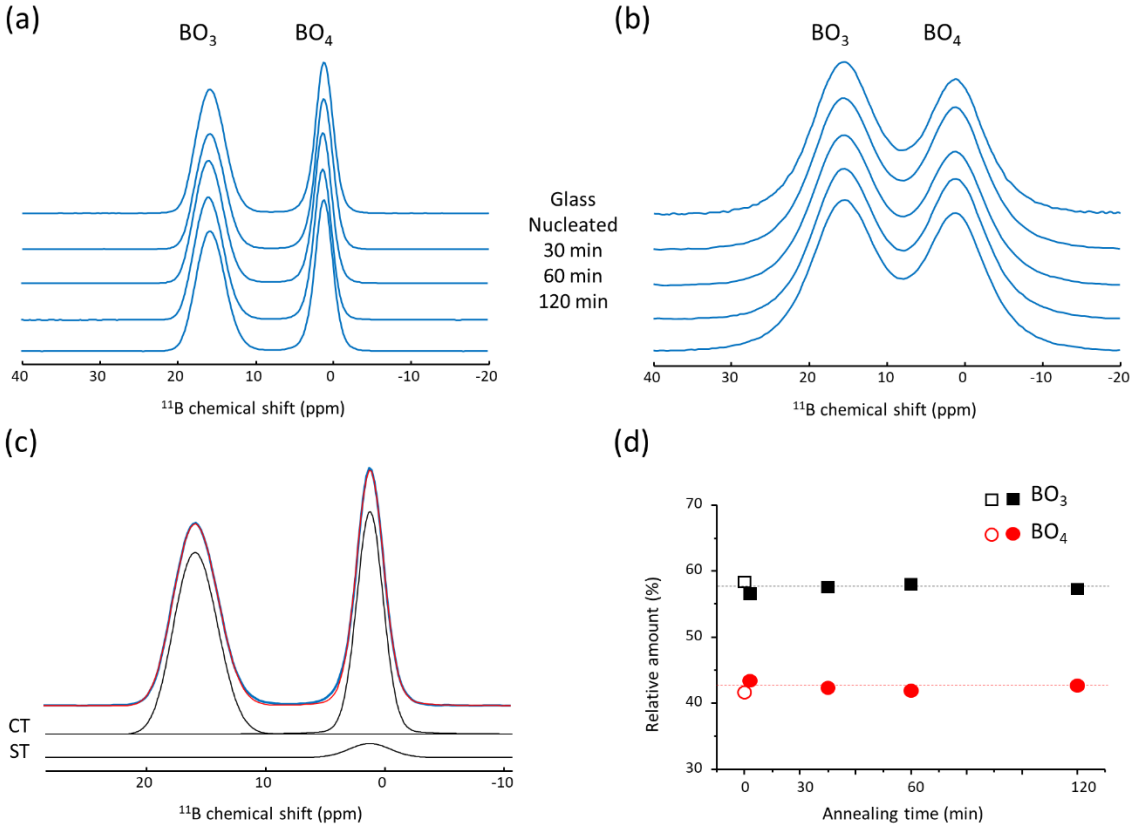

Figure 6: ^{11}B MAS NMR spectra recorded at 20 T of the (a) undoped and (b) Er^{3+}-doped materials. The spectra of the quenched glass, nucleated glass, nucleated and heat-treated during 30, 60 and 120 min at 450°C are shown from top to bottom in (ab). (c) Experimental (blue) and simulated (red) ^{11}B MAS spectrum of the undoped glass recorded at 20 T. Individual contributions corresponding to ^{11}B central (CT) and satellite (ST) transitions are shown as black lines. (d) Evolution of the relative proportion of BO_3 and BO_4 units in the

quenched glass (open symbols), nucleated glass and after annealing at 450°C during 30 up to 120 min (filled symbols). Details of spectrum simulations, as well as relevant tables, are given in supplementary information (Figure S2 + Tables S1 and S2).

Microstructural characterizations by Scanning and Transmission Electron Microscopies

Based on the XRD data, only the microstructure of the three GC samples (namely 45 min, 1h and 2h) was observed by SEM (Cf. top part of **Figure 7**). One can immediately see that the surface does indeed reflect the GC nature of the samples, as it is composed of crystalline entities (first, their shape is typical and TEM observations will further comfort this point), dispersed within some matrix (which will prove to be a glassy matrix). With the increase of the heat treatment duration at 450°C, from 45 min up to 2h, the density and size of these crystalline entities neatly increase: in particular, after 2h at 450°C, the individual size will reach dimensions beyond 1 μm. Such microstructural observations then fully explain the evolution of the visual aspect of the samples evidenced later in **Figure 12**. Finally, as the SEM images were recorded using backscattered electrons, it is important to stress that they are therefore sensitive to any change in the average electronic weight: this aspect will be further commented in light of the TEM investigations.

As stated in the experimental section, the surface crystalline fraction (supposed here to be representative of the volume crystalline fraction) was estimated via image analyses conducted using the ImageJ software [24]. Black and White binary images were generated in order to be processed, and the fraction of the crystalline entities was in fact translated into a percentage of crystals present at the surface. The latter is then indicated in the bottom part of **Figure 7** (see insert), as a function of the duration of the growth treatment at 450°C.

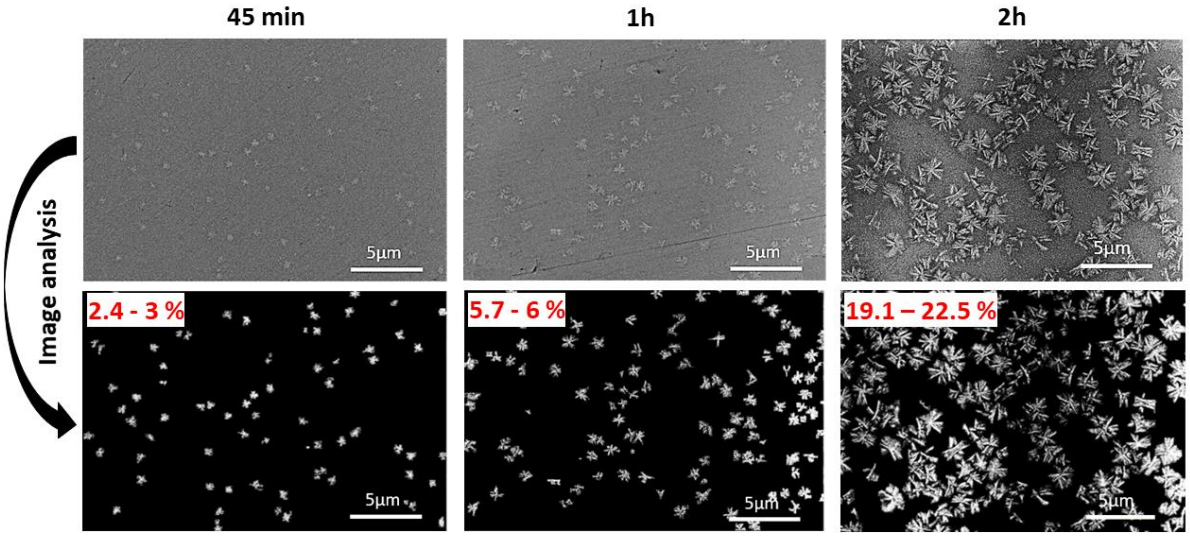

Figure 7: Top part: Backscattered SEM images of the three glass-ceramics elaborated by heat treatment conducted at the growth temperature, during 45 min, 1h and 2h, respectively. Bottom part: White and Black (WB) binary images generated during the image analysis of each surface in order to extract the percentage of the crystalline fraction. The surface crystalline percentage is indicated in insert of each WB image. The image analysis was run twice for each image: the slightly different results illustrate the dispersion in the estimation.

The TEM image (**Figure**) clearly reveals that the nucleated glass is completely homogeneous, so as the parent glass (not shown here). Thus, no glass-glass phase separation is observed, which agrees perfectly with the transparency of the glass (refer to **Figure 12** further). Such observation concords well with the work of Kaschieva *et al*. [11], as the composition under study should normally fall within the so-called "one-phase" glass region. As well, even at a larger magnification (right image on **Figure 8**), it appears that there are no clear traces of any nuclei formed. Moreover, the corresponding SAED pattern testifies to its amorphous nature, which is perfectly in agreement with the XRD analysis (Cf. **Figure 4-a**).

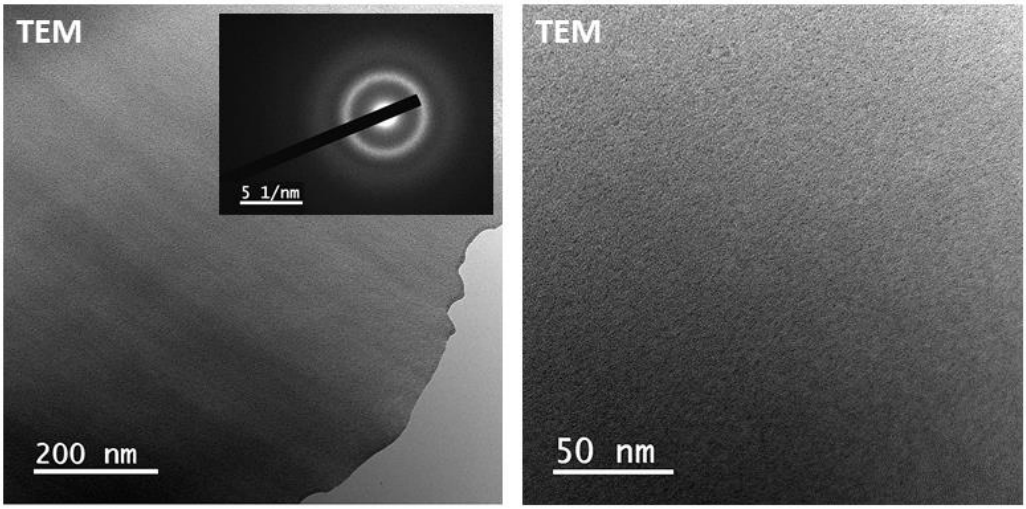

Figure 8: Bright field TEM images of the nucleated glass (heat treatment: 2h at 405°C, under air) at smaller (left) and larger (right) magnifications. Insert: corresponding SAED pattern.

The glass-ceramic sample produced after the combination of the nucleation (2h at 405°C) and growth (1h at 450°C) steps was also observed by TEM. As displayed in **Figure -a**, the sample can be described as darker entities dispersed in a brighter matrix. For this sample, the size of these entities ranges approximately from 600 up to more than 800 nm. Moreover, the shape of these entities nicely matches with the SEM macroscopic observations and the microstructure of each entity somehow resembles to that of a dendritic growth process. The corresponding SAED pattern recorded on such entity testifies to its "polycrystalline" nature (**Figure -b**). In fact, such entities resemble more to the superposition of several crystallites having different orientations, but for ease of reading, they will be simply qualified as "polycrystals". Moreover, the indexation of the diffracted spots matches well with the presence of the $Bi_2Te_2O_7$ structure, in agreement with the XRD data. The residual brighter matrix is also analyzed and the corresponding SAED pattern confirms its expected amorphous state (insert of **Figure -a**). Hence, the glass-ceramic contains polycrystalline entities dispersed in what appears as a homogenous amorphous matrix. Finally, in TEM mode, the full interpretation of the dark contrast observed for such polycrystals requires to obviously consider the Bragg contrast, but

as well to analyze the local chemical composition. Thus, in STEM mode, the contrast is proportional to the average atomic number Z and to the density: the brighter areas will reflect the presence of heavier elements (larger Z value), whereas the darker areas will correspond to regions containing lighter elements (smaller Z value). In **Figure 9-c**, polycrystals appear brighter than the vitreous matrix and therefore are richer in heavy elements. Finally, dark domains are present just at the surrounding of the polycrystals (pointed out by the white arrows in **Figure 9-c**), in comparison with the contrast of the rest of the residual glass matrix.

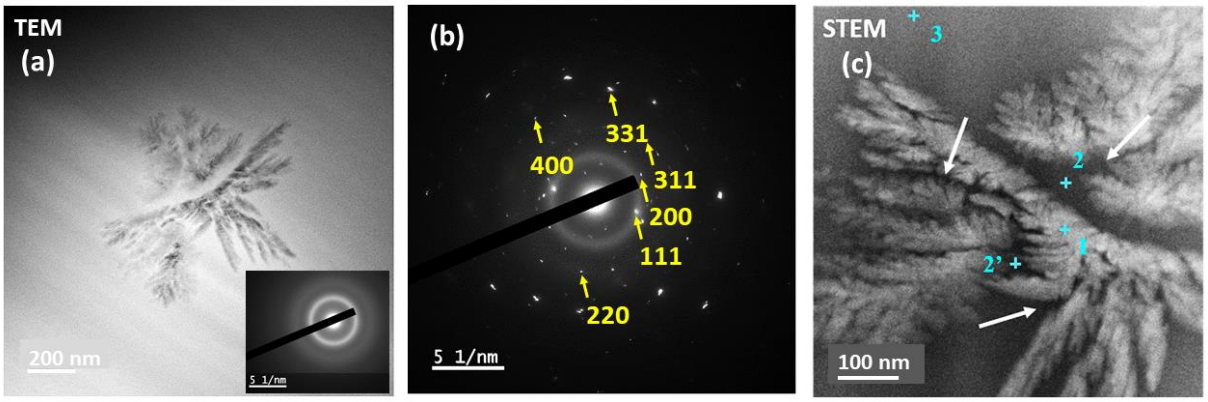

Figure 9: Observation of the glass-ceramic sample obtained after nucleation and growth during 1h at 450°C: (a) Bright field TEM image of one polycrystal dispersed in the residual glass matrix. The insert shows the SAED pattern characteristic of the amorphous matrix. (b) SAED pattern of this polycrystal, with some diffracted spots indexed using the $Bi_2Te_2O_7$ crystal structure (yellow arrows). (c) HAADF-STEM image (zoom) of the same polycrystal, with the white arrows showing the dark domains surrounding the polycrystal and the blue crosses pointing to the location of the conducted EDS measurements.

In order to be more quantitative, the Bi/Te ratio was determined in four different regions of interest via punctual EDS analyses, as highlighted by the blue crosses in **Figure 9-c**: (1) on the polycrystal, (2-2') on the darker areas surrounding the polycrystal, (3) somewhere further away from the polycrystal, in the residual amorphous matrix. The results are gathered in **Table 1**.

(a) Local probed area	Bi/Te ratio	(b) Theoretical value	Bi/Te ratio
Polycrystal (1)	1.2 ± 0.1	Nominal (initial) composition	2.0
Dark areas (2-2')	2.5 ± 0.2	$Bi_2Te_2O_7$	1.0
Residual matrix (3)	1.7 ± 0.2		

Table 1: (a) EDS elemental analyses: experimental determination of the local composition, via the Bi/Te ratio for the specific investigated zones: namely the polycrystal (1), the dark areas surrounding the polycrystal (2-2') and the residual glass matrix (3). (b) Theoretical Bi/Te ratio for the nominal glass composition and for the $Bi_2Te_2O_7$ crystalline phase. The error on the determination of the Bi/Te ratio is estimated to be about ± 10 %.

Firstly, considering the experimental errors, the local Bi/Te ratio of 1.2 ± 0.1 measured on the polycrystal (zone (1)) is close enough to 1, as expected with the crystallization of the $Bi_2Te_2O_7$ phase. Moreover, the small deviation from the ideal Bi/Te value of 1 might explain the moderate cell distortion deduced from the Rietveld refinement (Cf. **Figure 4b**). Secondly, the measured Bi/Te ratio on the residual glass matrix (zone 3) is found equal to 1.7 ± 0.2, which is not too far from the initial and nominal value of 2 for that composition. The third comment will concern the Bi/Te ratio of 2.5 ± 0.2 measured on the dark areas (zones 2-2') surrounding the polycrystal. At a first glance, these local EDS measurements appear completely in disagreement with the chemical contrasts observed the HAADF-STEM image (Cf. **Figure 9-c**). Indeed, the dark areas surrounding the polycrystal must correspond to regions of smaller Z value in average, therefore totally in contradiction with the Bi/Te ratio measured which is higher: bismuth is the heaviest element with Z = 83, whereas tellurium and boron elements have Z values respectively equal to 52 and 5. In addition, the polycrystal appears brighter which must match with a region of larger average Z value, once again in contradiction with the lowest value measured for the Bi/Te ratio. Obviously, EDS is not the appropriate technique to correctly quantify the boron content, because the latter is a too light element.

To fully understand the HAADF-STEM contrasts observed in **Figure 9-c**, it is mandatory to access the distribution of boron element. For this, EELS measurements were conducted at different locations to detect the boron repartition via the ionization edge (K-edge) of this element. As seen in **Figure -a**, two peaks characteristic of the presence of boron can be detected in the 190 – 210 eV energy range, only within the dark areas and the glassy matrix. At the opposite, the EELS data indicate that the boron signal is completely absent from the polycrystal, which is then in total agreement with the crystallization of the boron-free bismuth tellurite $Bi_2Te_2O_7$ phase. In order to have a more statistical information, some EELS map of the boron distribution has been recorded and is displayed in **Figure 10-d** (**Figure 10-b** corresponds again to the HAADF-STEM image of the same polycrystal, where the selected region to conduct the EELS spectrum-imaging is highlighted by the red square; **Figure 10-c** represents that particular zoom in the HAADF-STEM image, which defines the dimensions of the EELS spectrum-image). The red pixels in **Figure 10-d** testify to the presence of boron, whereas the dark pixels testify to its absence. Hence, it can be unambiguously proven that boron remains concentrated within the dark areas surrounding the polycrystals, and by extension also within the residual glassy matrix, whereas it is absent from the polycrystals. Therefore, the dark HAADF-STEM contrast results from the average between a high Bi/Te ratio (2.5 ± 0.2) and the high concentration of boron present in the corresponding areas. As well, on **Figure 9-c**, the grey tone of the residual glass matrix (further away from the polycrystals – zone (3)) results from the combination of an intermediate Bi/Te value (1.7 ± 0.2) and again the presence of boron. In order to fully justify the observed HAADF-STEM contrasts, the boron concentration would have to be lower in the residual glass matrix (further away from the polycrystals) compared to the concentration of boron at the dark areas surrounding the polycrystals. Obviously, this statement was not yet strictly demonstrated.

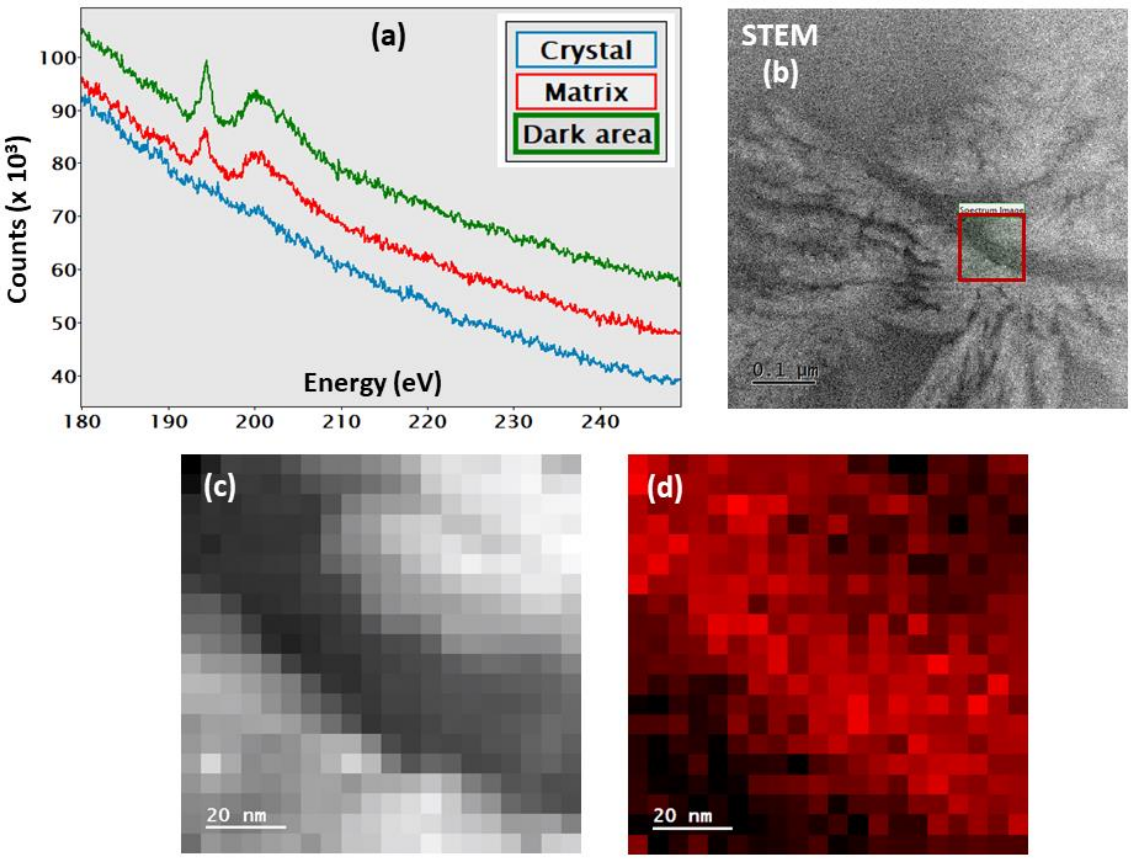

Figure 10: (a) EELS data collected at the Boron ionization edge (K-edge) for the different regions of interest: the polycrystal (blue curve), the residual glass matrix (red curve) and the dark areas corresponding to the regions around the polycrystal (green curve). (b) HAADF-STEM image of the same polycrystal previously displayed, with the selected region to conduct the EELS spectrum - imaging highlighted by the red square. (c) A zoom within this region and (d) the associated map showing the boron distribution: red pixels reveal its presence.

Based on all the aforementioned TEM data, it is finally possible to attempt proposing some crystallization mechanism. The EELS data prove that boron oxide clearly remains located only within the glassy matrix and around the polycrystals formed. Thus, the partial crystallization occurs concomitantly with, or even provokes, the observed chemical demixtion (in other words, the boron oxide phase separates from the bismuth tellurite crystal phase). A way of seeing the events could be to consider that with the formation of $Bi_2Te_2O_7$ polycrystals, the latter "simply"

expel the boron oxide, thus in agreement with the fact that there are no known crystalline oxide phase containing at the same time bismuth, tellurium and boron.

To slightly refine the global picture, EDS maps were also recorded in order to access simultaneously the distribution of both tellurium and bismuth elements. Thus, **Figure 11** displays the collected EDS maps, and it is very clear that polycrystals contain far more tellurium than their immediate contours (see **Figure 11-b**). As the surroundings of the polycrystals correspond to the dark areas where the boron oxide was found concentrated, again, this is another specific signature for the phase separation between boron oxide and tellurium oxide. And, regarding the spatial distribution of bismuth (**Figure 11-c**), polycrystals contain more Bi than their immediate surroundings, although the relative variation seems to be rather moderate. A last and specific comment regarding the EDS map recorded for the erbium element is given in supplementary information.

Finally, the EDS map recorded for tellurium (**Figure 11-b**) helps to better understand how it is possible to end up with a Bi/Te ratio close to 1 and by this way crystallize the $Bi_2Te_2O_7$ phase, while the initial Bi/Te ratio is equal to 2. In fact, the crucial physical parameter is the temperature, and the latter (450°C during the growth step) is certainly sufficient to provide the necessary mobility for the atoms. Hence, two things will likely happen concurrently, in relation with the limited chemical affinity between TeO_2 and B_2O_3, as discussed in the introduction:

- starting from the initial Bi/Te fraction equal to 2, if the Te concentration strongly increases locally, then this would explain how an experimental Bi/Te ratio of 1.2 ± 0.1 can be reached, leading as a consequence to the formation of the encountered polycrystals,
- starting from the same initial Bi/Te fraction equal to 2, if the Te concentration strongly drops locally, then this would explain how an experimental Bi/Te ratio of 2.5 ± 0.2 can be this time reached, giving basically birth to these darks area where the tellurium content is indeed supposed to be rather low.

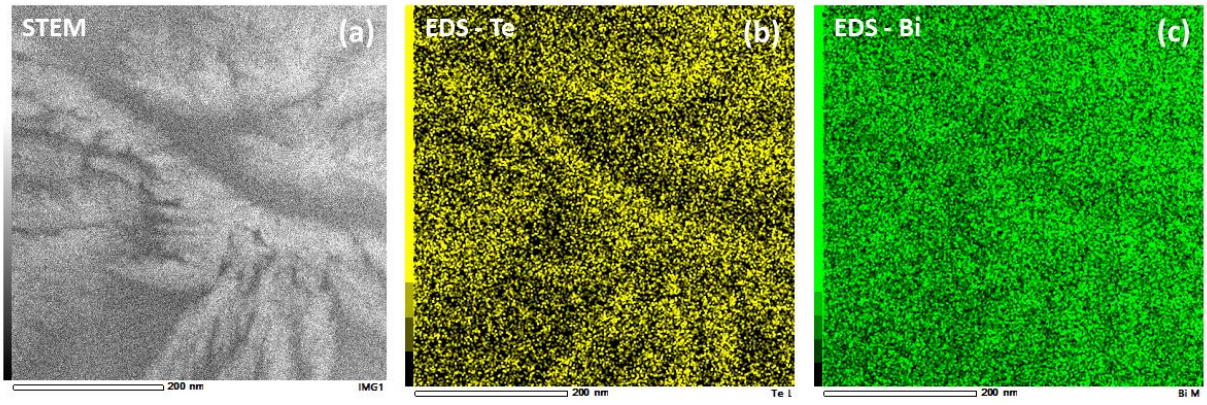

Figure 11: (a) HAADF-STEM image of the same polycrystal. (b) EDS maps revealing the spatial distribution of tellurium (presence shown in yellow) and (c) bismuth (presence shown in green) elements.

Optical properties

The optical transmission of all the investigated samples is plotted in **Figure** . The optical transparency of the nucleated glass is strictly identical to that of the parent glass (not shown here) and remains therefore optimal, which concords with the homogeneity evidenced by TEM at the local scale. With an increased duration of the growth heat-treatment, the transparency strongly drops, mostly in the visible range. If for the sample heat-treated for 1h at 450°C, the NIR transparency still reaches 65 to 70 % of the incident light, after 2h of heat treatment at the same temperature, the NIR transmission falls down to a maximum of 40 %. This degraded transparency is obviously the consequence of important light scattering effects which are correlated to the increase of the volume fraction of the aforementioned polycrystalline entities. As discussed already several times, these polycrystals correspond to the $Bi_2Te_2O_7$ phase, which has an orthorhombic crystalline symmetry (thus not cubic). In addition, such entities very likely present an important refractive index contrast with the residual glassy matrix, as intuited from the hugely different respective chemical compositions evidenced by the previous HAADF-

STEM images and EELS analyses. These two combined reasons will therefore induce important birefringence effects. As well, the band located around 3000 nm corresponds to the absorption provoked by the -OH groups for all samples [37]. Several other narrow absorption lines/bands are present from 400 until 2000 nm, attesting to the correct incorporation of erbium ions within the initial parent glass. Finally, as displayed in insert of **Figure 12**, the visual aspect of the samples fully corroborates the measured optical transparency data.

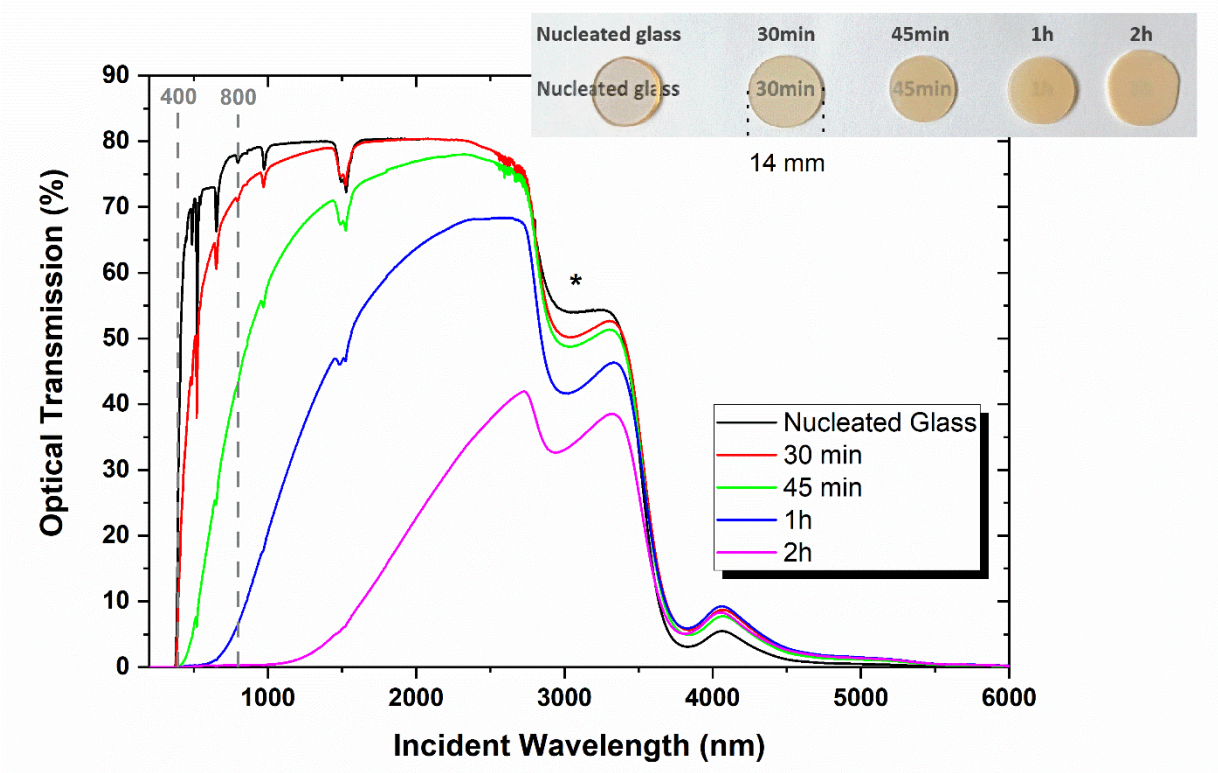

Figure 12: Optical transmission data measured from 200 up to 6000 nm for the samples of the TBB-Er composition (thickness ~ 0.7 mm). Please note that the transmission of the parent glass (not presented here) is strictly identical to that of the nucleated glass. The (*) symbol stands for the absorption provoked by the -OH groups. The visible spectral range is also highlighted. The photographs of the glass nucleated at 405°C during 2h, and of the samples submitted to a second growth treatment at 450°C during times ranging from 30 min up to 2h, are placed in insert of the figure. Their diameter is about 14 mm.

Figure 6 depicts both emission and excitation PL spectra collected at room temperature, for all the series of investigated samples (*i.e*. the nucleated glass, the sample heat-treated 30 min at 450°C and the three glass-ceramics samples). The spectra were all normalized, considering the maximum amplitude at 1530 nm (for the emission) or at 530 nm (for the excitation). According to the literature, following the excitation conducted using a wavelength of 978.5 nm, Er^{3+} ions undergo some desexcitation in particular through the well-known $^4I_{13/2}$ - $^4I_{15/2}$ electronic transition, leading to the emission of photons in the NIR, centered around 1535 nm [38-39]. Thereby, emission spectra were collected in the 1400 - 1650 nm range. One can directly see on **Figure 13-a** that the first spectral changes (at longer wavelengths) happen beyond 30 min of heat treatment at the growth temperature. Such evolution is fully consistent with the first signs of crystallization detected by XRD after 45 min of heat treatment at 450°C. The excitation spectra were then measured for an emission wavelength fixed at 1535 nm. **Figure 6-b** shows that these excitation spectra are composed of many transitions from the ground state $^4I_{15/2}$ to the excited states $^4I_{11/2}$, $^4I_{9/2}$, $^4F_{9/2}$, $^4S_{3/2}$, $^2H_{11/2}$, $^4F_{7/2}$, $^4F_{5/2}$, $^4F_{3/2}$, $^3H_{9/2}$ and $^2G_{11/2}$ [39]. Interestingly, among them, the $^4I_{15/2}$-$^2G_{11/2}$ transition at 378 nm is considered as being hypersensitive, *i.e*. very sensitive to even minute changes happening in the direct surrounding around Er^{3+} ions [39]. There is indeed some important and continuous modification of the PL intensity of this band, with the increased duration of the heat treatment, reflecting the strong and progressive modification of the environment around rare earth ions.

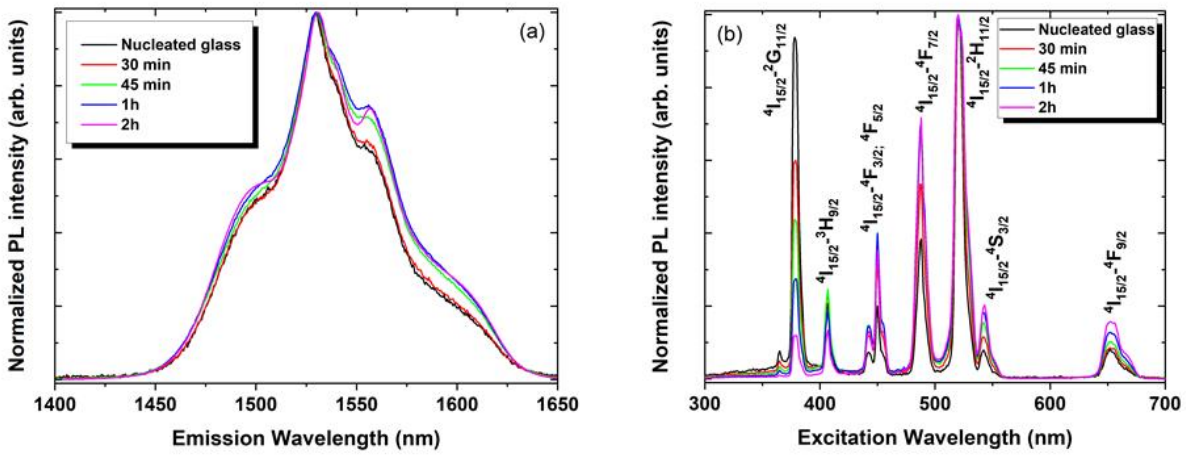

Figure 6: (a) Normalized PL emission spectra associated with the $^4I_{13/2}$ - $^4I_{15/2}$ electronic transition (λ_{exc} = 978.5 nm) and collected for five samples (the nucleated glass and the samples heat-treated at 450°C for 30 min, 45 min, 1h or 2h). (b) Normalized PL excitation spectra (λ_{em} = 1535 nm) collected for the same series of samples and displayed in the 300-700 nm range (both the $^4I_{15/2}$-$^4I_{11/2}$ and the $^4I_{15/2}$-$^4I_{9/2}$ transitions are outside this range).

Finally, every PL decay curves were measured (data not shown here). For the nucleated glass sample, as well as for the two samples respectively produced after 30 and 45 min of heat treatment at 450°C, it is noteworthy that it was possible to correctly model the PL decay curve using a single exponential decay function, with a good quality of the fit, reflected by a r^2 value > 0.997. Beyond that heat treatment duration, as the volume crystalline fraction increases (Cf. **Figure 7**), it is necessary to introduce a second exponential decay function to properly fit the PL decay curves. This perfectly reflects the two different environments for Er^{3+} ions, statistically localized within the glass matrix or within the $Bi_2Te_2O_7$ polycrystals. However, such approach of using the sum of two exponential decay functions presents some considerable limitations, in the sense that it is difficult to correctly constrain the fit to the data, leading then to important mistakes either for the fitted lifetimes values or for the fitted amplitudes. Therefore, for our samples, the effective average lifetime value $< \tau >$ of the $^4I_{13/2}$ excited state was

calculated using the following equation [40] in order to better depict the evolution of the distribution of sites for Er^{3+} ions:

$$< \tau > \ = \frac{\int_0^t I(t).t.dt}{\int_0^t I(t).dt}$$

Figure 7 finally plots the evolution of this effective average lifetime, as a function of the duration of the heat treatment at 450C° (the nucleated glass corresponds to a dwell time equals to zero min). Up to 45 min of crystallization at 450°C, the lifetime remains constant to a value equal to ~ 0.88 ms, once more in agreement with the XRD data which revealed the early stages of crystallization after this heat treatment duration. Beyond that, the lifetime starts increasing neatly to reach ~ 0.99 ms and ~ 1.74 ms respectively after 1h and 2h of heat treatment, thus in perfect agreement with the macroscopic XRD data and with the increase in the volume crystallization fraction evidenced by SEM. Again, these results reflect the modification of the environment around the rare earth ions that takes place with the partial crystallization. Besides, it should be noticed that the lifetime value measured for the nucleated glass is of the same order of magnitude than some values reported in the literature, like for instance in the case of erbium doped calcium borotellurite glasses [41].

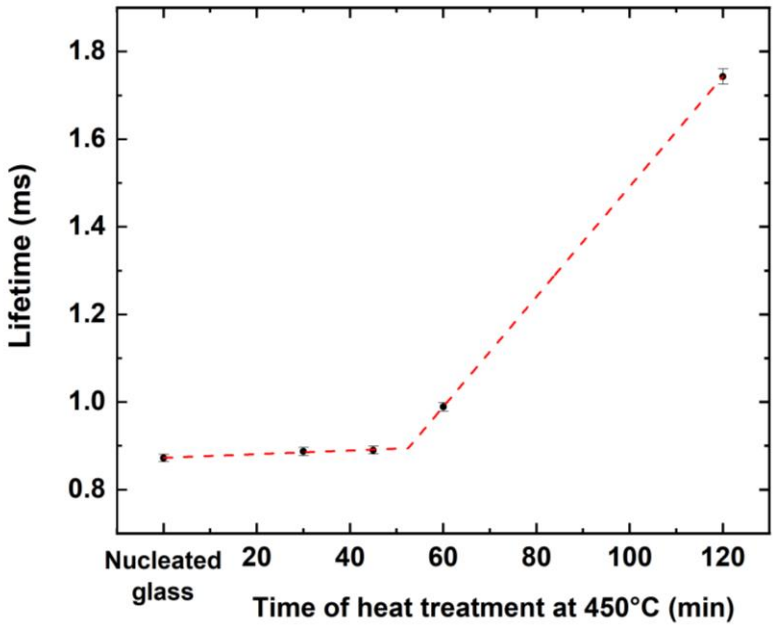

Figure 7: Effective average lifetime values extracted from PL decay curves (λ_{em} =1535 nm, λ_{exc} = 978.5 nm) for the five samples under investigation: namely the nucleated glass (2h at 405°C), and samples heat treated at 450°C during 30 min, 45 min, 1h or 2h. The error bars are maximized and estimated to be about ± 1%. The red dashed curve serves only here as a guide for the eyes to highlight the tendency discussed in the body of the paper.

CONCLUSION

Starting from an initial homogeneous glass of the composition $30TeO_2$-$40B_2O_3$-$30Bi_2O_3$ doped with $0.5Er_2O_3$, new borotellurite glass-ceramics containing $Bi_2Te_2O_7$ crystals were successfully synthesized, after conducting a two-step heat-treatment: nucleation at 405°C during 2h, and growth at 450°C for at least 45 minutes. Based on macroscopic SEM and local TEM/STEM observations, the final glass-ceramic microstructure can be described as a volumic distribution of $Bi_2Te_2O_7$ polycrystalline dendritic formations randomly dispersed in a glassy matrix: their size and density increase with the growth treatment time. Local chemical analysis (EDS and EELS measurements, HAADF-STEM imaging) performed by transmission electron microscopy allowed accessing the spatial repartition of bismuth, tellurium and boron elements

at the nanoscale. All these data combined together makes it possible to propose a crystallization mechanism of these $Bi_2Te_2O_7$ entities, which is therefore directly connected to the occurrence of the chemical demixtion. Locally, boron oxide is somehow "expelled" from the boron-free $Bi_2Te_2O_7$ phase, which to be formed, requires to monopolize larger concentrations of TeO_2 than the initial one. Consequently, the immediate surrounding of the just formed polycrystals is strongly impoverished in TeO_2, and simultaneously strongly enriched in boron oxide. Additionally, both Raman spectroscopy and NMR data revealed that the nature and ratio of the borate structural units within the residual glassy matrix do not seem to really evolve during the partial crystallization. The presence of Er^{3+} ions in the composition finally allows exploring the photoluminescence properties of such borotellurite materials. Though only moderate spectral changes were observed for the NIR emission, the partial crystallization clearly generated consequent modifications around the rare-earth ions, as testified by the strong variations of the excitation spectra. As well, the evolution of the lifetime of the $^4I_{13/2}$ excited level is almost multiplied by a factor of two between 45 minutes and 2h of heat treatment at 450°C, reflecting once more the considerable structural modifications undergone around Er^{3+} ions.

One prospect will be obviously to understand the exact role of the nucleation step played in the partial crystallization, as this aspect of this work remains so far an open question. As well, within such TeO_2-B_2O_3-Bi_2O_3 system, other glass compositions showing initial chemical demixtion immediately after quenching will be now explored again in the aim to fabricate another type of new glass-ceramic materials.

AUTHOR INFORMATION

Corresponding Author

Jean René Duclère, email: jean-rene.duclere@unilim.fr

Author Contributions

The manuscript was written through contributions of all authors. All authors have given approval to the final version of the manuscript.

Funding Sources

This work has been financially supported by institutional grants from the Agence Nationale de la Recherche (ANR): namely the LabEX SigmaLim (ANR-10-LABX-0074-01) and TRAFIC (ANR-18-CE08-0016-01) projects. As well, this work was supported by the Nouvelle-Aquitaine Region via the MON ECOLE project (AAPR2021-2020-11934110). This work was also partially granted by the ANR through the project (ANR-23-CE08-0013-01). It has also benefited from the microscopy facilities of the Platform MACLE-CVL which was co-funded by the European Union and Center-Val de Loire Region (FEDER). Financial support from the IR INFRANALYTICS FR2054 for conducting the research is also gratefully acknowledged.

Notes

The authors declare no competing financial interest.

REFERENCES

[1] R. A. H. El-Mallawany, *Tellurite Glasses Handbook: Physical Properties and Data*, CRC Press, 2012, Second Edition.

[2] Caffey, D., Radunsky, M. B., Cook, V., Weida, M., Buerki, P. R., Crivello, S., Day, T. *Recent results from broadly tunable external cavity quantum cascade lasers*. Proc. SPIE 7953 (2011), 79531K.

[3] V. A. G. Rivera, D. Manzani Editors, "*Technological Advances in Tellurite Glasses: Properties, Processing and Applications* », *Springer Series in Materials Science*, 2017, 254.

[4] P. Patra, K. Annapurna, *Transparent Tellurite Glass-Ceramics for photonics applications: A Comprehensive Review on crystalline phases and crystallization mechanisms*, Progress in Mater. Sci., 125 (2022) 100890.

[5] Y. Dimitriev, E. Kashchieva, *Immiscibility in the TeO_2-B_2O_3 system*, J. Mater. Sci., 10 (1975) 1419-1424.

[6] H. Borger, W. Vogel, V. Kozhukharov, M. Marinov, *Phase equilibrium, glass-forming, properties and structure of glasses in the TeO_2-B_2O_3 system,* J. Mater. Sci., 19 (1984) 403-412.

[7] E. Kashchieva, P. Hinkov, Y. Dimitriev, S. Miloshev, *Microaggregation processes in B_2O_3-TeO_2 glasses*, J. Mater. Sci. Lett., 13 (1994) 1760-1763.

[8] E. P. Kashchieva and Y. B. Dimitriev, *Unusual Immiscibility Structures in Tellurite Glasses,* J. Am. Ceram. Soc., 80 (1997) 1588–1590.

[9] S. Bhattacharyya, T. Hoche, N. Hemono, M. J. Pascual, P. A. van Aken, *Nano-crystallization in LaF_3–Na_2O–Al_2O_3–SiO_2 glass*, J. Cryst. Growth, 311 (2009) 4350–4355.

[10] S. Chenu, E. Véron, C. Genevois, G. Matzen, T. Cardinal, A. Etienne, D. Massiot, M. Allix*, Tuneable Nanostructuring of Highly Transparent Zinc Gallogermanate Glasses and Glass-Ceramics,* Adv. Optical Mater., 2 (2014**)** 364–372.

[11] E. Kashchieva, M. Pankova, Y. Dimitriev, *Liquid Phase Separation in the Systems TeO_2-B_2O_3-M_2O_3 (M_2O_3 = Al_2O_3, Ga_2O_3, Sc_2O_3, La_2O_3, Bi_2O_3)*, Ceramics – Silikáty, 45 (2001) 111-114.

[12] T. Hasegawa, *Optical properties of Bi_2O_3–TeO_2–B_2O_3 glasses*, *J. Non-Cryst. Solids*, 357 (2011) 2857-2862.

[13] G. Zhao, Y. Tian, H. Fan, J. Zhang, L. Hu, *Properties and Structures of Bi_2O_3-B_2O_3-TeO_2 Glass*, J. Mater. Sci. Technol., 29 (2013) 209-214.

[14] A. Kaur, A. Khanna, H. Bhatt, M. Gónzález-Barriuso, F. González, B. Chen, M. N. Deo, *B-O and Te-O speciation in bismuth tellurite and bismuth borotellurite glasses by FTIR, ^{11}B MAS-NMR and Raman spectroscopy*, J. Non-Cryst. Solids, 470 (2017) 19–26.

[15] Y. B. Saddeek, K. A. Aly, K. S. Shaaban, A. M. Ali, M. M. Alqhtani, A. M. Alshehri, M. A. Sayed, E. A. Abdel Wahab, *Physical properties of B_2O_3–TeO_2–Bi_2O_3 glass system*, J. Non-Cryst. Solids, 498 (2018) 82–88.

[16] Y. Anantha Lakshmi, K. Swapna, S. Mahamuda, M. Venkateswarlu, A. S. Rao, *Photoluminescence properties of Sm^{3+} ions doped Bismuth Borotellurite glasses*, Solid State Sci., 116 (2021) 106609.

[17] A. Amat, H. M. Kamari, I. Mansor, N. Osman, N. N. S Nidzam, N. I. M. Kamal, *Comparative spectroscopy study of TeO_2– B_2O_3 glass system for photonic application: barium and bismuth as modifier*, Appl. Phys. A, 127 (2021) 792.

[18] N. Elkhoshkhany, R. Abbas, R. El-Mallawany, S. F. Hathot, *Optical properties and crystallization of bismuth boro-tellurite glasses*, J. Non-Cryst. Solids, 476 (2017) 15–24.

[19] K. S. Shaaban, E. S. Yousef, *Optical properties of Bi_2O_3 doped boro tellurite glasses and glass ceramic*s, Optik - International Journal for Light and Electron Optics, 203 (2020) 163976.

[20] M. H. A. Mhareb, M. A. Morsy, Hana Almarri, M. I. Sayyed, I. Alrammah, N. Alonizan, Y. S. M. Alajerami, Q. A. Drmosh, M. Kh Hamad, G. N. Makhadmeh, M. A. Almessiere, *Gamma-ray induced effect on the structural and optical properties and durability of*

neodymium-doped zinc–bismuth–borotellurite glasses and glass ceramics, Opt. Mater., 137 (2023) 113572.

[21] M. Cholin, C. Genevois, P. Carles, J. Cornette, S. Chenu, M. Allix, G. Delaizir, P. Thomas, V. Couderc, J.-R. Duclère, *Highly transparent bismuth borotellurite glass-ceramics: Comprehension of crystallization mechanisms*, J. Non-Cryst. Solids, 598 (2022) 121953.

[22] Petricek, V., Dusek, M. & Palatinus, L., *Crystallographic Computing System JANA2006: General features*, Z. Kristallogr., 229 (2014) 345-352.

[23] Amoureux, J. P.; Fernandez, C.; Steuernagel, S., *Z filtering in MQMAS NMR*, J. Magn. Reson. Ser. A, 123 (1996) 116-118.

[24] Schneider, C.A. *et al.*, *NIH Image to ImageJ: 25 years of image analysis*, Nature Methods, 9 (2012) 671-675.

[25] Höland, W., Beall, G.-H., *Glass-Ceramic Technology*, John Wiley & Sons, 2nd edition, 2012, 448 pages.

[26] H. E. Kissinger, *Reaction Kinetics in Differential Thermal Analysis*, Anal. Chem., 29 (1957) 1702-1706.

[27] A. Marotta, A. Buri, F. Branda, *Nucleation in glass and differential thermal analysis*, J. Mater. Sci., 16 (1981) 341-344.

[28] C. S. Ray, D. E. Day, *Determining the Nucleation Rate Curve for Lithium Disilicate Glass by Differential Thermal Analysis*, J. Am. Ceram. Soc., 73 (1990) 439-442.

[29] K. S. Ranasinghe, C. S. Ray, D. E. Day, *A generalized method for determining the crystal nucleation and growth rates in glasses by differential thermal analysis*, J. Mater. Sci., 37 (2002) 547-555.

[30] X. Hu, G. Guery, J. D. Musgraves, D. VanDerveer, J. Boerstler, N. Carlie, P. Wachtel, S. Raffy, R. Stolen, K. Richardson, *Processing and characterization of transparent TeO_2–Bi_2O_3–ZnO glass ceramics*, J. Non-Cryst. Solids, 357 (2011) 3648-3653.

[31] A. Bertrand, J. Carreaud, G. Delaizir, M. Shimoda, J.-R. Duclère, M. Colas, M. Belleil, J. Cornette, T. Hayakawa, C. Genevois, E. Veron, M. Allix, S. Chenu, F. Brisset, P. Thomas, *New transparent glass-ceramics based on the crystallization of "anti-glass" spherulites in the Bi_2O_3-Nb_2O_5-TeO_2 system*, Cryst. Growth Des., 15 (2015) 5086-5096.

[32] D. Mercurio, J. C. Champarnaud-Mesjard, I. Gouby, B. Frit, *On the crystal structure of $Bi_2Te_2O_7$*, Eur. J. Solid State Inorg. Chem., 35 (1998) 49-65998.

[33] O. Durand, *Propriétés structurales et vibrationnelles des phases désordonnées dans le système TeO_2-Bi_2O_3*, Thèse de l'Université de Limoges, 2006.

[34] A. E. Miller, K. Nassau, K. B. Lyons, M. E. Lines, *The intensity of Raman scattering in glasses containing heavy metal oxides*, J. Non-Cryst. Solids, 99 (1988) 289-307.

[35] G. Lakshminarayana, S. O. Baki, A. Lira, I. V. Kityk, M. A.Mahdi, *Structural, thermal, and optical absorption studies of Er^{3+}, Tm^{3+}, and Pr^{3+}-doped borotellurite glasses*, J. Non-Cryst. Solids, 459 (2017) 150–159.

[36] C. P. E. Varsamis, N. Makris, C. Valvi, E. I. Kamitsos, *Short-range structure, the role of bismuth and property–structure correlations in bismuth borate glasses*, Phys. Chem. Chem. Phys., 2021, 23, 10006.

[37] D. C. Harris et M. D. Bertolucci, *Symmetry and Spectroscopy: An Introduction to Vibrational and Electronic Spectroscopy*, Dover Publications, INC., New York. 1989.

[38] P. Hänninen, H. Härmä, *Lanthanide Luminescence: Photophysical, Analytical and Biological Aspects*, Springer Science & Business Media, 2011.

[39] F. Auzel, *Contribution à l'étude spectroscopique de verres dopés avec* Er^{3+} *pour obtenir l'effet laser*, Ann. Télécommunications, 24 (1969) 199-229.

[40] E. Nakazawa, "Fundamentals of luminescence," in *Phosphor Handbook*, S. Shionoya and W.M. Yen, Eds., p. 104, CRC Press, Boca Raton, Fla, USA, 1999.

[41] J. F. Gomes, A. M. O. Lima, M. Sandrini, A. N. Medina, A. Steimacher, F. Pedrochi, M. J. Barboza, *Optical and spectroscopic study of erbium doped calcium borotellurite glasses*, Opt. Mater., 66 (2017) 211-219.